Experimental wind-tunnel study of the dynamics of inverted foils for energy harvesting

M. Flores Salinas[1], R.M. Botez[1] , M. Tavallaeinejad[2] and M.P. Païdoussis[2]

[1]Laboratoire de recherche en commande active, avionique et aéroservoélasticité, École de Technologie Supérieure, Montréal, Québec, Canada and [2]Department of Mechanical Engineering, McGill University, Montréal, Québec, Canada
Corresponding author: R. M. Botez; Email: ruxandra@gpa.etsmtl.ca

Abstract

This paper describes the methodology used to analyse oscillations of foils of a wide range of aspect ratios, $0.5 \leq AR \leq 4$, and Reynolds numbers, $10^4 \leq Re \leq 10^5$, for energy harvesting purposes. The foils were fixed at their trailing edge, and their dynamical behaviour was captured as the wind speed was varied. The foil response was then analysed as a function of velocity, Reynolds number, oscillation amplitude and frequency. Additionally, the forces and moments acting on the foils were measured, utilising an aerodynamic scale, designed and built in-house. An empirical power generation equation was derived to determine the foil characteristics for maximum energy harvesting production. The results show that a flexible foil with $AR = 3$ with oscillations in the large-amplitude regime is the most effective for energy harvesting.

Nomenclature

A	oscillation amplitude
AR	foil aspect ratio
B	deflection rigidity
d	dimensionless amplitude
E	Young's modulus
f	vortex shedding frequency
F_x, F_y	foil force components
H, L, h	foil height, length, thickness
Kb	bending stiffness ratio
LE	foil leading edge
l/L	foil dimensionless deflection
$\Delta l/L$	dimensionless tip deflection
M_x, M_y	foil moment components
TE	foil trailing edge
$\bar{P}$	power extracted
P_t	fluid total pressure
P_s	fluid static pressure
q_c	fluid dynamic pressure
PDF	probability density function
PSD	power spectral density
Re	Reynolds number
St	Strouhal number
U	flow velocity

μ	mass ratio
ν	kinematic viscosity
ν_p	Poisson's ratio
ρ_s	foil density
ρ_f	fluid density, air density
$w(L,t)$	foil displacement
$\dot{w}(L,t)$	foil velocity

1.0 Introduction

Renewable energy production that can function for extended periods of time and reduce the need for batteries is of major concern in the modern world [1–3]. A great deal of effort has been expended towards developing self-powered devices that can capture energy from oscillating foils and convert it into energy [4–6]. A flexible foil immersed in a fluid flow can experience self-induced periodic oscillations at various flow velocities. The oscillation of foils is of interest not only because of its occurrence in nature, but also because it can generate great amounts of clean renewable energy, even with relatively small-sized foils [7–9].

In this research, we consider cantilevered foils exclusively, with a clamped trailing edge (TE), a free leading edge (LE) and no other support elsewhere. This configuration is referred to as the "inverted foil configuration". The flow direction is parallel to the rest position of the foil, and is presumed to be uniform and steady, as shown in Fig. 1. The 2D representation shows the length (L) and height (H) of the foil and the mean flow speed U direction.

Analytical and experimental studies on conventional plates in axial flow were performed by Guo and Païdoussis [10] who employed inviscid potential flow theory to predict the onset of oscillatory instability. They were the first to conclude that the plates oscillate at critical velocities inversely proportional to their mass ratio.

In 2013, the first experimental investigation on inverted foil flapping was conducted by Kim et al. [11] who identified three flow regimes, namely, with the foil straight, undergoing large-amplitude flapping and fully deflected. Additionally, they reported that the foil mass ratio has little effect on the onset of large-amplitude flapping.

In a 2016 study by Sader et al. [12], it was found that two key parameters of the dynamics of inverted foils are the foil's length (L) and height (H). For foils, where L is at least 10 times H, they found that foils do not flap, but they go from the straight mode (a) to the fully deflected mode (f) shown in Fig. 2. Additional dynamical states have been identified in that and subsequent studies [12–15] as a function of flow velocity and foil aspect ratio. For sufficiently large aspect ratio, as shown in Fig. 2, the foil (a) is straight, (b) is buckled, undergoes (c) small-amplitude asymmetric flapping, (d) large-amplitude flapping, (e) aperiodic or chaotic flapping and (f) becomes fully deflected.

In this paper, we analyse the dynamics of inverted foils over a wide range of foil aspect ratios, $0.5 \leq \text{AR} \leq 4$, in the Reynolds number regime of $10^4 \leq \text{Re} \leq 10^5$, in well-defined and controlled experimental tests. The inverted foil configuration was chosen in this research because: (i) inverted foils are more susceptible to instabilities at various flow conditions and can exhibit more flapping modes; (ii) an inverted foil configuration can produce energy several times larger than a conventional-foil configuration for the same foil size [16–19].

As stated earlier, the overall motivation for this research is to investigate the dynamics of inverted foils as an efficient energy harvesting system. This method of renewable energy production requires fluid kinetic energy to be transferred to the foil (as strain energy), and then the strain energy to be converted into energy with an "energy generator mechanism" that will rotate a motor shaft. The "energy generator mechanism" design and validation is part of a future study by the present authors. The Power $\bar{P}$ extracted from the "energy generator mechanism" is equivalent to the extracted energy from foil oscillations. As there is no actuation system, the input energy is null, and thus the net energy extracted is always
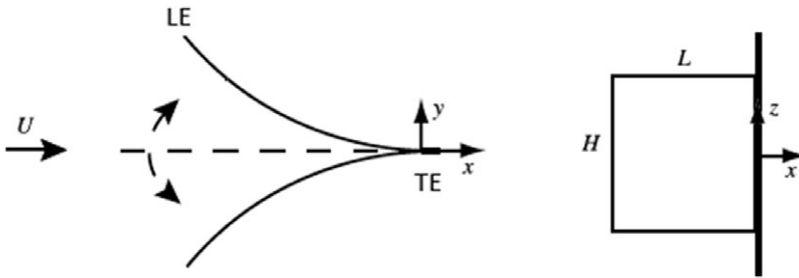
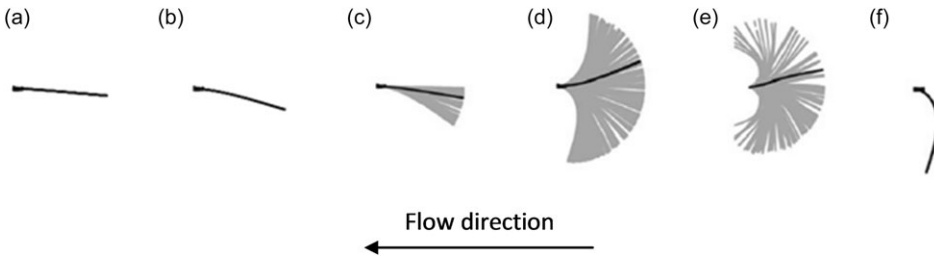**Figure 1.** *Physical parameters of an inverted foil configuration.*

Figure 2. *Experimental measurement of a foil clamped at the trailing edge (inverted foil configuration) in axial flow. The direction of the flow is from right to left, as shown by the arrow. The foil is black and its recorded path is grey. The foil dynamics shows the followings modes: (a) straight, (b) buckled, (c) small-amplitude asymmetric flapping, (d) large-amplitude flapping, (e) aperiodic or chaotic flapping and (f) fully deflected state. Data collected and image produced in Matlab version 9.0 (R2016a).*

guaranteed to be positive. The extracted energy from an oscillating foil can be determined using the empirical equation of Mitcheson et al. [20],

$$\overline{P} \approx A \, \text{St}^3. \tag{1}$$

where $\overline{P}$ is the extracted power, A is the oscillation amplitude, and St is the Strouhal number.

The research objectives in this paper are the following.

(1) Investigate the effects of foil length and height (aspect ratio), flapping frequency, flapping regime, Strouhal number, Reynolds number and foil peak-to-peak amplitude.
(2) Analyse the characteristics of inverted foils for power generation.
(3) Analyse the forces acting on inverted foils for a better understanding of foil dynamics and power generation.

2.0 Definitions of dimensionless parameters

We consider a foil of length L, height H, density ρ_s, thickness h, in fluid flow of density ρ_f and flow velocity U. The aspect ratio AR, mass ratio μ, and Reynolds number are defined by Kim et al. [11]

$$\text{AR} = \frac{H}{L}, \; \mu = \frac{\rho_f \, L}{\rho_s \, h}, \; \text{Re} = \frac{U \, L}{\nu}, \tag{2}$$

where ν is the fluid kinematic viscosity.

A dimensionless amplitude of oscillation is defined by Kim et al. [11]

$$d = \frac{A}{L},$$ (3)

where A is the maximum peak-to-peak amplitude.

We also define a parameter Kb as defined by Kim et al. [11]

Bending stiffness Kb is the ratio of the deflection rigidity B of the foil and the fluid inertia, as shown by Equation (4a). The fluid inertia is defined by the fluid density ρf, with a specific flow velocity U and foil length L, as shown in Fig. (4b). The deflection rigidity B, which is the force required to bend a flexible foil, it is defined by the Young's modulus E, the thickness of the foil h, and the Poisson' ratio of the foil material defined by the variable v. deflection rigidity B is calculated as shown by Equation (4c).

$$Kb = \frac{\text{Deflection rigidity}}{\text{Fluid inertia}}$$ (4a)

$$Kb = \frac{B}{\rho f \, U^2 \, L^3}$$ (4b)

$$B = \frac{E \, h^3}{12(1 - v^2)}$$ (4c)

Also, presuming that vortex shedding from the deformed upstream end of the foil occurs, we define the Strouhal number as shown in Equation (5) from the work of Mitcheson et al. [20]

$$\text{St} = \frac{fA}{U},$$ (5)

where f is the vortex shedding frequency in Hz.

3.0 Apparatus and instrumentation

The experimental tests were performed in the Price-Païdoussis (P-P) subsonic wind tunnel of the Research Laboratory in Active Controls, Avionics and Aeroservoelasticity (LARCASE). New methodologies in the aeronautical field have been developed at the LARCASE, including computational fluid dynamics (CFD) model validations with experimental results from subsonic wind tunnel tests [21–30].

The properties of the inverted foils, the novel design of the aerodynamics scale, the P-P wind tunnel, as well as the real-time data acquisition system and instrumentation used in this research are described in this section.

3.1 Foil properties

Foils made of various metal and plastic materials were tested in the wind tunnel. Brass foils were found to give asymmetric oscillation and undergo permanent deformation. Zinc foils were found to have a high material damping and could not flap at all. Stainless steel and propylene foils had other problems [13]. Polycarbonate foils were found to behave best, and they were chosen for the experiments to be described. Table 1 lists the properties and dimensions of the foils used.

3.2 Experimental setup

For the study and analysis of foil dynamics in the inverted foil configuration, a novel design was developed in-house of an aerodynamic scale for measuring forces and moments, along the three axes oriented

Table 1. *Material and geometric properties of the foils tested in the wind tunnel*

Foil Properties	
Material	Polycarbonate
Young's Modulus E	2.38GPa
Poisson ratio v	0.38
Foil density ρ_s	1,200Kg m^{-3}
Foil aspect ratio	AR $= 0.50$
(Length $\times$ Height $\times$ Thickness)	$(150 \times 75 \times 1.02)\ 10^{-3}$m
Foil aspect ratio	AR $= 0.75$
(Length $\times$ Height $\times$ Thickness)	$(150 \times 112.5 \times 1.02)\ 10^{-3}$m
Foil aspect ratio	AR $= 1$
(Length $\times$ Height $\times$ Thickness)	$(150 \times 150 \times 1.02)\ 10^{-3}$m
Foil aspect ratio	AR $= 2$
(Length $\times$ Height $\times$ Thickness)	$(150 \times 300 \times 1.02)\ 10^{-3}$m
Foil aspect ratio	AR $= 3$
(Length $\times$ Height $\times$ Thickness)	$(150 \times 450 \times 1.02)\ 10^{-3}$m
Foil aspect ratio	AR $= 4$
(Length $\times$ Height $\times$ Thickness)	$(150 \times 600 \times 1.02)\ 10^{-3}$m
Air density ρ_f	1.225Kg m^{-3}
Mass ratio μ	$\mu = 0.15$
$\rho_f \times$ Length/($\rho_s \times$ Thickness)	$1.225 \times 150/(1200 \times 1.02)$

Figure 3. *Inverted foil aerodynamic scale for forces and moments measurements: (a) side view; (b) left view.*

parallel and perpendicular to the foil's surface and parallel to the foil's height. The parts of this aerodynamic scale are illustrated in Fig. 3. The novel clamping screw mechanism uses 27 flat-head screws and 2 symmetrical NACA 0012 aerofoils to support the inverted foil at the trailing edge, without obstructing the flow. An important characteristic of this design is that the clamping screw mechanism and the strain gauge sensors are mechanically aligned and joined together with a coupling mechanism which allows all forces and moments on the foil's surface to be transmitted to the aerodynamic scale. This unique
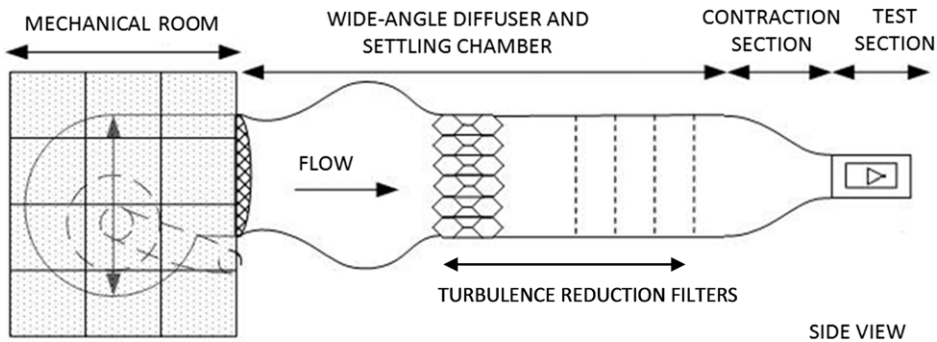
Figure 4. *Price-Païdoussis Wind Tunnel schematic.*

clamping and coupling mechanism makes it possible to measure and record the foil's displacement (by a high-speed camera), and to simultaneously measure and record the forces and moments acting on the foil. The aerodynamic scale has a measured drag coefficient of only $C_d = 0.008$ for an angle-of-attack AoA $= 0°$.

For each flow speed, the foil displacement, forces and moments were recorded simultaneously. The interface plate allows for positioning the aerodynamic scale inside the test-section without interfering with the incoming flow. The foil's clamping and the coupling mechanism were machined from high strength aluminum alloy 606. This aerodynamic scale can measure *Fx, Fy* and *Fz* forces of up to 290N and moments *Mx, My* and *Mz* of up to 10N m, with a full-scale accuracy of 1/8N and 1/19N m, respectively. The output signals, of the measured forces and moments on all three axes, were amplified, filtered, and sent to the data acquisition system for recording and treatment.

3.3 Wind tunnel

The Price-Païdoussis open-return subsonic wind tunnel consists of a centrifugal fan, a diffusing and settling chamber, a contraction section, and a test-chamber or test section, as shown in Fig. 4. The air enters the wind tunnel by two inlets located on opposite sides of the centrifugal fan. The engine and the centrifugal fan are located in the mechanical room, and they are protected from dust particles by filters in an enclosed area. The main parameters to characterise the flow during wind tunnel tests are: (i) the total, static and dynamic pressures; (ii) the temperature variation during the test; (iii) the controlled flow speed; and (iv) the Reynolds number. The turbulence reduction air filters with honeycomb cell shape and squared cell shape (black dashed lines) can be seen in the settling chamber in Fig. 4; their main function is dissipating and reducing the flow turbulence to a value below 1% [31]. The experiments took place in the test-section with height $\times$ width $\times$ length of $0.62 \times 0.91 \times 1.83$m.

The flow velocity in the test-section was determined by a Pitot tube. The mean flow speed *U* was determined for a temperature of 22°C and using the air density ρ_f and the difference between the total pressure P_t and the static pressure P_s, as stated in Equation (6) [31]:

$$P_t - P_s = q_c = \frac{1}{2}\rho_f U^2.$$
(6)

Figure 5 shows an inverted foil in the wind tunnel setup for the experiments. The foil trailing edge TE was fixed, and the leading-edge LE was free.

3.4 High-speed camera

Measurements were made using a FLIR Systems high-speed camera. This camera has a global shutter, minimising "blur effects" on moving objects. It operates at 163fps at a maximum resolution of $1,920 \times$
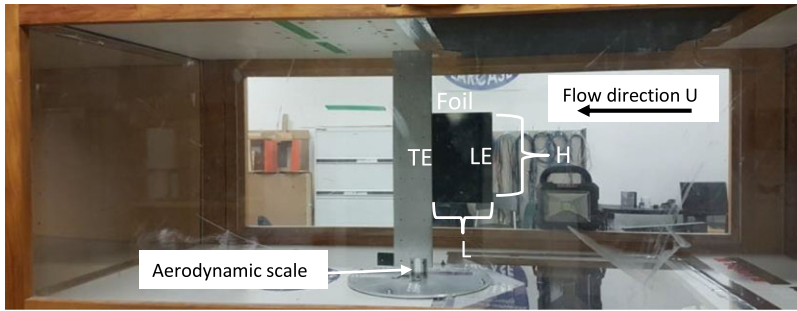
Figure 5. *Side view of an inverted foil configuration mounted in a wind tunnel.*

1,200 pixels; the exposure time range can vary between 0.005ms to 31.98s [32]. This exposure time range is sufficient to capture approximately 16 frames for a typical cycle of foil flapping. A fixed focal length lens was set on the image sensor. The camera system enables multiple points painted at the leading edge of the foils to be traced. These points help to determine the foil's displacement in real-time. A MATLAB image-processing script was developed in-house for extracting the displacements of the foils from the video images. The leading edge slope of the foil was determined, using a linear fit. A point at the leading edge of the foil was used to determine the foil's transverse and longitudinal deflections. The length of each foil at rest was used as the reference image for calibration.

3.5 Data acquisition system

A multifunction data acquisition system (DAS) from National Instruments (NI), USB-6210, was chosen to convert the analog signals of the aerodynamic scale into digital data, and to save the post-processed data. The USB-6210 allows measurements of up to 16 analog inputs and does not require external power for its functioning. A video was recorded for each flow speed, from 5.0 to 18.4m/s with an increment of 0.2m/s, to capture the foil's displacement. The high resolution and high frequency video signals were also sent to the data acquisition system for data treatment and post-processing. This data acquisition system made it possible to record the signal from the aerodynamic scale and the video signal simultaneously and in real-time. The sampling rate was 300Hz for the foil's displacement videos and 1,000Hz for the forces and moments.

The data collected from the videos, as well as the forces and moments, were imported with a hardware timing resolution of 50ns [33] using an in-house MATLAB script (version 9.0-2016b) for the analysis in the post-processing phase.

4.0 Results

In this section, a combination of empirical analysis and wind tunnel measurements is used to establish the relation between foil dynamics and energy production [34, 35]. The time history of tip displacement recorded during the wind tunnel tests, the displacement at a specific flow speed (probability density function), the dominant frequencies (power spectral density) and the phase-plane portrait are used to analyse the foil dynamics.

There are three regimes of dynamic behaviour for a foil with AR < 0.1: (i) stretched-straight, (ii) flapping and (iii) fully deflected, as observed by Sader et al. [12]. For foils with AR ≥ 0.2, the recent work of Tavallaeinejad et al. [36] has identified three other regimes, for a total of six possible foil dynamical states. In this paper, we use the regimes identified in [36] to classify foil deflection at different flow speeds.

(i) The stretched-straight regime with small vibrations superimposed

(ii) The buckled regime, involving a small mean deflection with small-amplitude random-like vibrations superimposed

(iii) The small-amplitude regime with coherent, periodic oscillations around the deflected equilibrium

(iv) The large-amplitude flapping regime

(v) The aperiodic (chaotic) regime with intermittent flapping around the origin and to one side

(vi) The fully deflected regime

The next sub-sections present the experimental data, analyse the inverted foil deflections, describe the inverted foil's dynamics regimes and analyse the forces produced by the inverted foils.

Figure 6. *Time history (a) and PDF (b) of the tip displacement of $AR = 1$ foil for $U = 5.0 m/s$.*

Figure 7. *Time history (a) and PDF (b) of the tip displacement of $AR = 1$ foil for $U = 7.0 m/s$.*

4.1 Oscillations of the $AR = 1$ inverted foil

The first experimental data presented are those of the square-shaped foil ($AR = 1$), with $H = L = 150$mm. This foil will be the reference foil, utilised to assess if a more slender or a wider foil is better suited for energy harvesting.

At very low airflow speeds, between 5.0 and 7.0m/s, the foil stays in a stable undeformed equilibrium, parallel to the incoming flow without any oscillation, as shown in Figs. 6(a) and 7(a). The quasi-Gaussian form of the probability density function (PDF) plots suggests small random oscillations, induced by turbulence and unsteadiness of the incoming flow, as shown in Figs. 6(b) and 7(b).

Increasing the flow speed in the wind tunnel test chamber to 7.5 and 7.9m/s causes the $AR = 1$ foil to buckle slightly and exhibit random oscillations with small amplitudes. As shown in Fig. 8(a), the tip
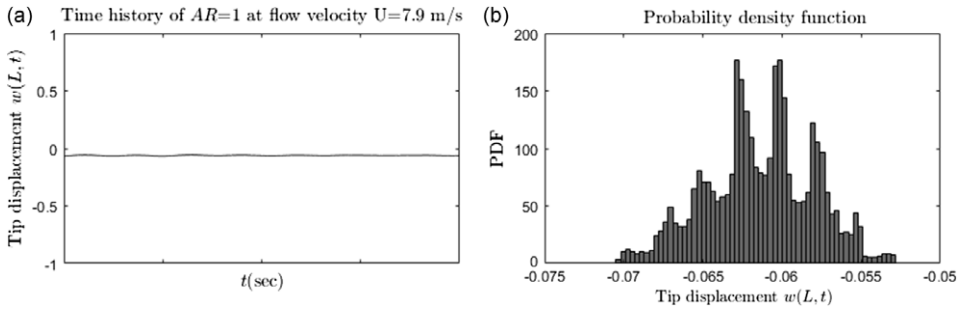
Figure 8. *Time history (a) and PDF (b) of the tip displacement of AR = 1 foil for U = 7.9m/s.*

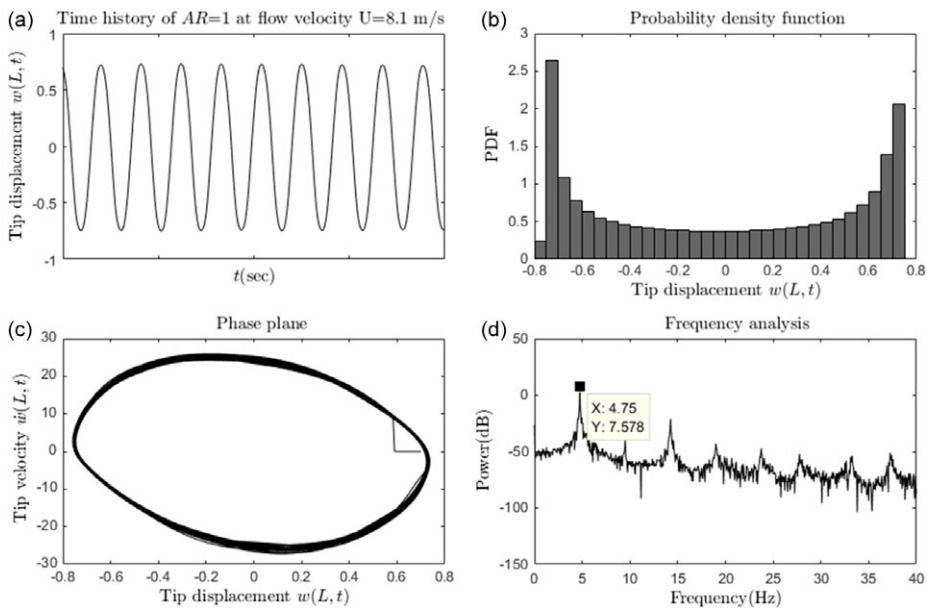**Figure 9.** *Time history (a), PDF (b), phase-plane (c) and frequency (d) of the tip displacement of AR = 1 foil for U = 8.1m/s.*

displacement time history is very small, and the probability density function shows a small oscillation between 0.055L and 0.065L for $U = 7.9$m/s in Fig. 8(b).

Increasing the wind speed to 8.1m/s, the foil started flapping abruptly, with an amplitude of 0.8L and a frequency of 4.75Hz, as seen in Fig. 9(a) and (d). The double mast and convex shape of the probability density function and the single-loop response of the phase-plane portrait indicate a periodic oscillation of the foil, as shown in Fig. 9(b) and (c), respectively.

For flow speeds ranging from 8.5 to 10.5m/s, the flapping transverse amplitude reached 0.8L, with a flapping frequency decreasing from 4.85 to 4.6Hz (refer to Figs. 10 and 11). The phase-plane plots show that the large-amplitude flapping is predominantly periodic, as does the classical double-masted shape of the PDFs, with a transition to a damped behaviour of the foil deflections, as the flow speed increases.

As the air flow speed is increased to 11.0m/s, the transverse deflection response of the inverted foil shows an interesting feature with double peaks, marked by a dotted circle in Fig. 11. The double peaks can be detected in the time history and probability density function of Figs. 11(a) and (b). These double peak responses indicate that the foil undergoes extremely large-amplitude bending with the tip slope
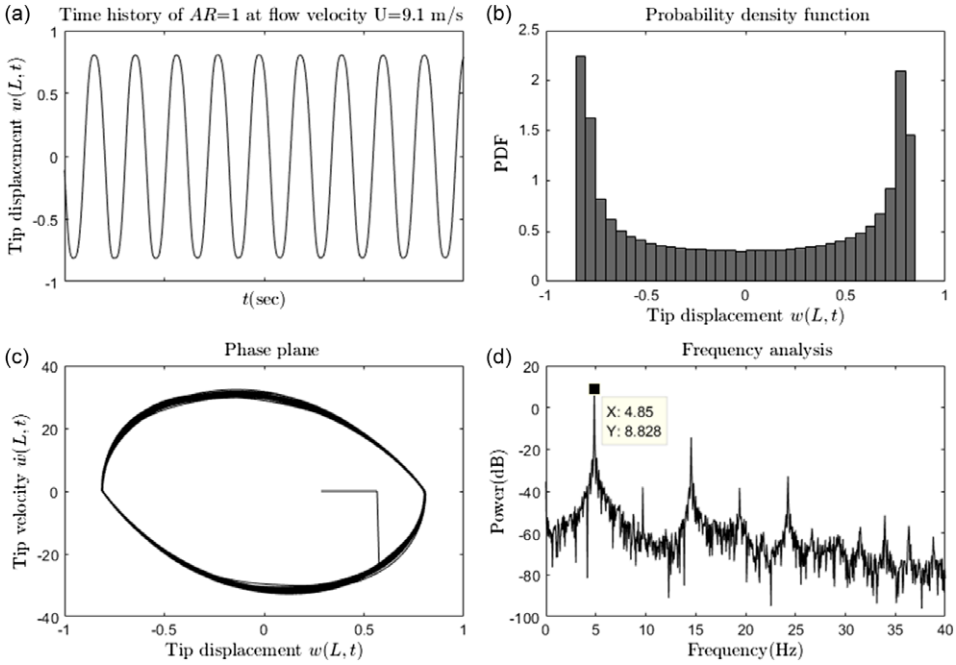
Figure 10. *Time history (a), PDF (b), phase-plane (c) and frequency (d) of the tip displacement of AR = 1 foil for U = 9.1m/s.*
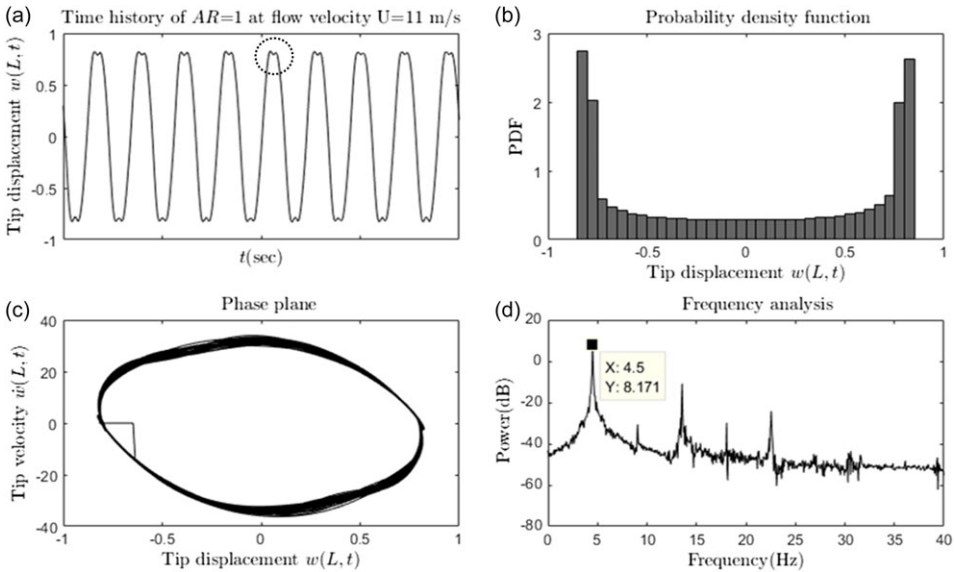

Figure 11. *Time history (a), PDF (b), phase-plane (c) and frequency (d) of the tip displacement of AR = 1 foil for U = 11.0m/s.*
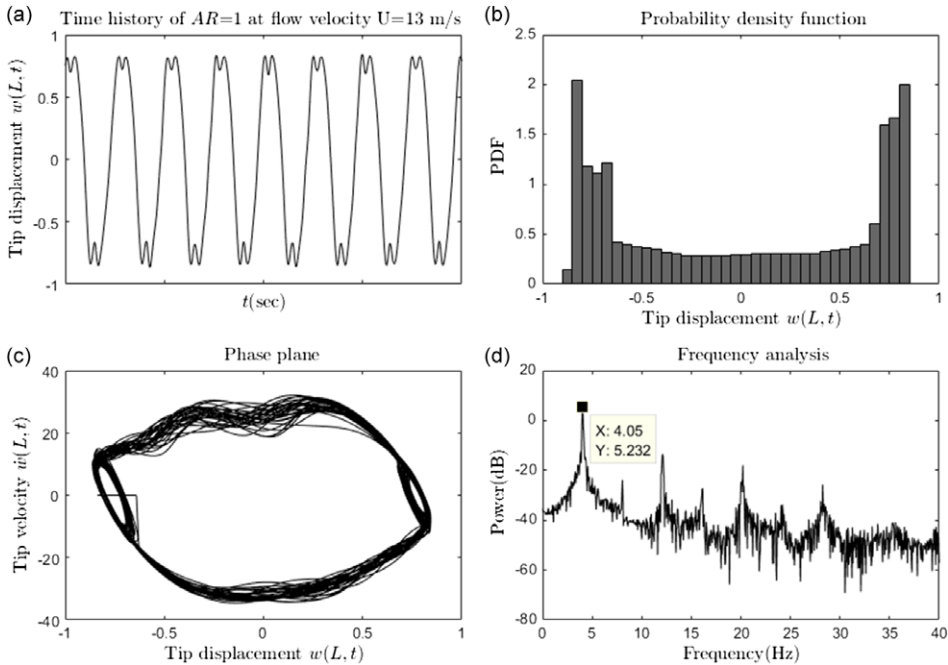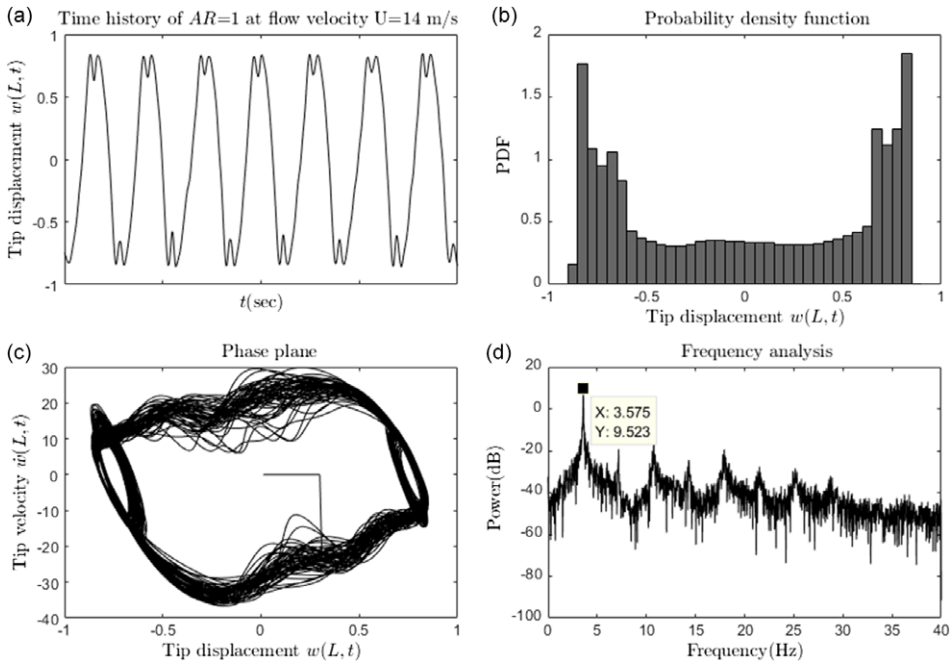
Figure 12. *Time history (a), PDF (b), phase-plane (c) and frequency (d) of the tip displacement of AR = 1 foil for U = 13.0m/s.*

going beyond 90 degrees. As a result, the transverse deflection displays local minima. This indicates that the flapping amplitude continues to increase as the wind speed increases as shown in Fig. 11(c). In Fig. 11(d), the frequency domain (power spectral density plot) shows higher harmonics contributing to the system response.

For the flow speed range of $12.0 \leq U \leq 13.5$m/s, the oscillation frequency is reduced from 4.25 to 3.8Hz. Figure 12 shows the chaotic regime characteristics (tip displacement, PDF, phase-plane and power spectral density) of the AR = 1 foil for U = 13m/s.

For flow speed higher than 13m/s (as seen on Fig. 13, for 14m/s), the two peaks at the edge of the foil oscillation have increased in size and the oscillation is no longer periodic; the inverted foil is considered in a chaotic regime. Sader *et al.* [12] were among the first to identify the chaotic regime of an inverted foil. The definition given was "*when the foil transitions from a periodic, large-amplitude flapping regime to an aperiodic flapping regime, it is considered a chaotic regime*".

It can be noted in Fig. 13(a)–(d) for U = 14m/s, while the flapping amplitude is still ∼0.8L, the dominant frequency of the inverted foil's oscillation decreases to 3.575Hz and the phase-plane no longer shows a periodic shape. At the flow speed critical value higher than 14.0m/s, the foil displays a one-sided deflected shape, showing the fully deflected regime identified by Kim et al. [11], and any oscillation will cease suddenly.

4.2 Dynamic regimes of AR = 1 inverted foil

Figure 14 shows the various transitions in dynamical state that the AR = 1 inverted foil undergoes are: (a) quasi-static state with very low amplitude oscillation (less than 0.1L, where L is the foil length) for $U < 8.0$m/s corresponding to Re $< 8 \times 10^4$; (b) flapping, with amplitude 0.85L for $U > 8.0$m/s; (iii) cessation of flapping at $U \approx 14.0$m/s.

Figure 13. *Time history (a), PDF (b), phase-plane (c) and frequency (d) of the tip displacement of AR = 1 foil for U = 14.0m/s.*
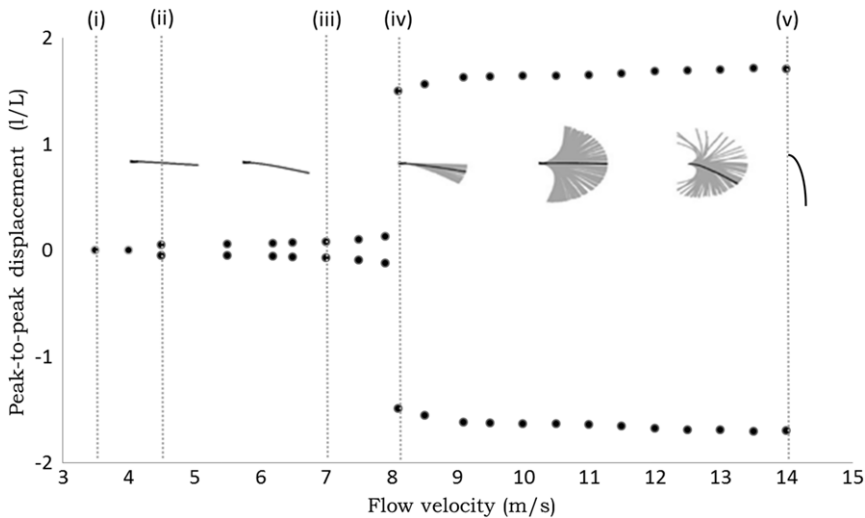

Figure 14. *Bifurcation of Poincaré points for the AR = 1 foil.*

A more refined classification of these dynamical states is given as follows: (i) totally static, (ii)–(iii) quasi-static with small oscillations; (iii)–(iv) asymmetric flapping; (iv)–(v) large amplitude flapping; beyond (v) cessation of flapping. In the range 13.0m/s $<U<$ 14.0m/s, the oscillation is aperiodic (chaotic), with the flapping occurring more often on one side than on the other.

Figure 15. *Strouhal number of function of flow velocity for the AR = 1 foil.*

The Strouhal number (St) variation with the U for the inverted AR $= 1$ foil is provided in Fig. 15. A non-zero St occurs once oscillation (flapping) takes place. With increasing flow velocity, St decreases from St $= 0.140$ to St $= 0.063$.

4.3 Oscillations of the AR < 1 inverted foils

The phase-plane and PSD diagrams of a foil of AR $= 0.5$ are shown in Fig. 16.

For $U = 9.8$m/s, the foil undergoes small oscillations as seen in Fig. 16(a) and (b), then it exhibits large-amplitude oscillations for $U = 10.0$m/s in Fig. 16(c) and (d), aperiodic oscillations for $U = 16.7$m/s in Fig. 16(e) and (f) and chaotic oscillations for $U = 18.5$m/s in Fig. 16(g) and (h).

The corresponding results for a foil of AR $= 0.75$ are shown in Fig. 17.

For $U = 9.8$m/s, as seen in Fig. 17(a) and (b), the foil undergoes small oscillations. At $U = 11.6$m/s, as seen in Fig. 17(c) and (d), the large-amplitude regime is observed with a single-loop in the phase-plane diagram and a dominant frequency of 5.2Hz in the power spectral density (PSD) diagram. At $U = 17.1$m/s, as seen in Fig. 17(e) and (f), the foil oscillations are irregular with a reduced and not well defined (not prominent) flapping frequency of $\approx$2Hz. At $U = 18.8$m/s, as seen in Fig. 17(g) and (h), the foil fully deflects to one side and ceases oscillating.

4.4 Oscillations of the AR > 1 inverted foils

In this section, we explore the dynamic regimes of foils whose heights are two, three and four times their lengths, AR $= 2$, AR $= 3$ and AR $= 4$, respectively.

Figure 18 shows the experimental data and different oscillation regimes obtained for the AR $= 2$ foil for three flow speeds $U = 8.0$, 8.78 and 16.6m/s. Small-amplitude oscillations around the zero (neutral) position can be seen in Fig. 18(a) and (b) for $U = 8.0$m/s. Large-amplitude oscillations, with a well-defined "single-loop" phase–plane shape and a dominant frequency of 5.3Hz are seen in Fig. 18(c) and (d) for $U = 8.78$m/s. The ill-defined shapes on the phase-plane and the absence of a dominant frequency are signs of a chaotic regime, as observed in Fig. 18(e) and (f) for $U = 16.6$m/s.

At a flow speed U of 7.1 m/s, the AR $= 3$ foil starts showing small-amplitude oscillations behaviour, as seen in Fig. 19(a) and (b). As soon as the flow speed reaches 7.6m/s, the large-amplitude oscillations start showing a very well-defined phase-plane shape and a dominant frequency of 5.2Hz, as seen in Fig. 19(c) and (d). Then, a chaotic regime follows at $U = 16.2$m/s, as seen in Fig. 19(e) and (f).

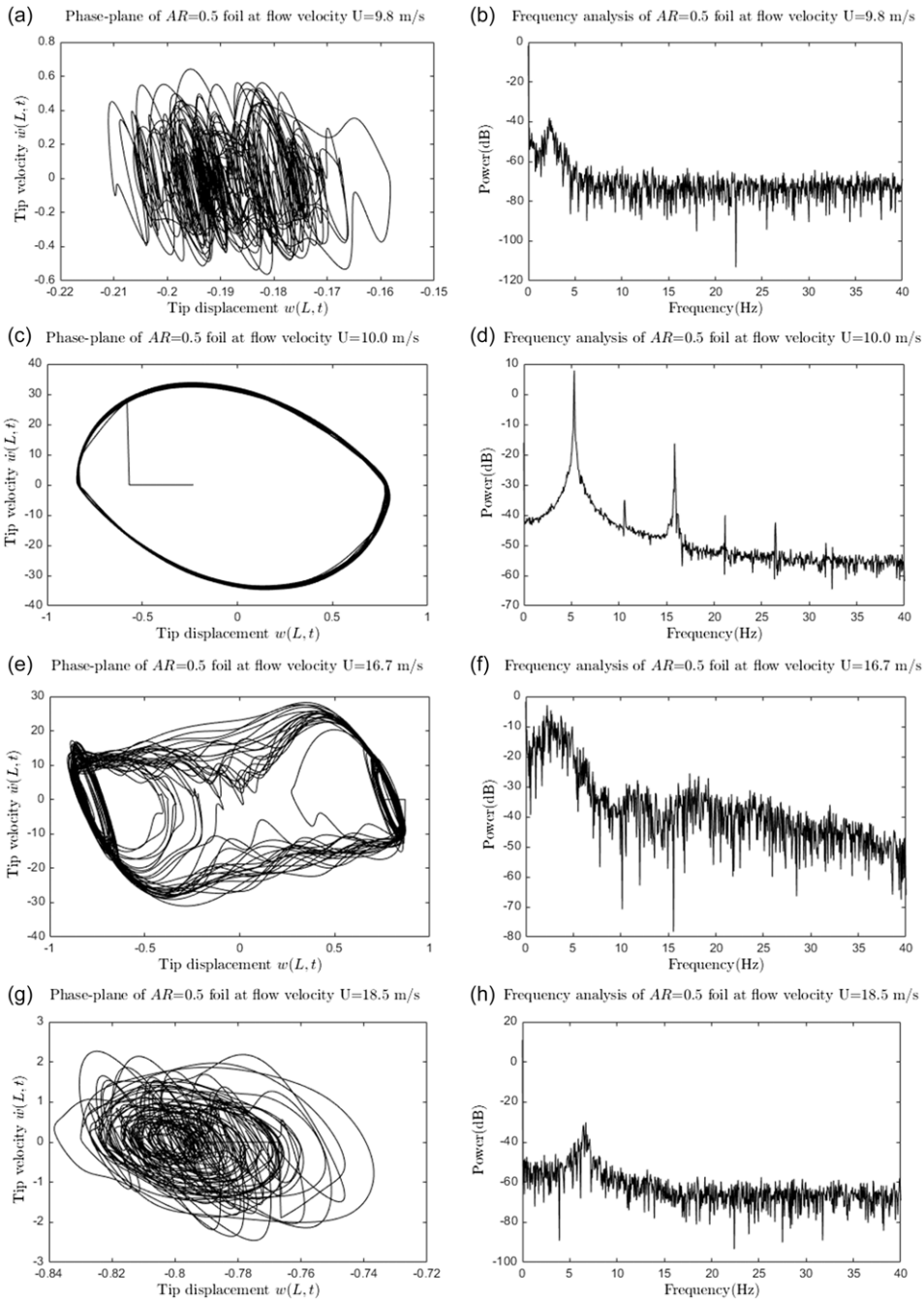**Figure 16.** *(a,b) Phase-plane and frequency of AR = 0.50 foil for U = 9.8m/s; (c,d) for U = 10.0m/s; (e,f) for U = 16.7m/s; and (g,h) for U = 18.5m/s.*

The last foil tested had an aspect ratio AR = 4. The small-amplitude oscillations and the phase-plane shapes are not periodic with a dominant frequency of 2.7Hz for U = 7.0m/s is not well-defined, as observed in Fig. 20(a) and (b). At a flow speed of 9.0m/s, the single-loop phase-plane shape and the dominant frequency of 5.7Hz are signs of a periodic oscillation, as seen in Fig. 20(c) and (d). At and

Figure 17. *(a,b) Phase-plane and frequency of AR = 0.75 foil for U = 9.8m/s; (c,d) for U = 11.6m/s; (e,f) for U = 17.1m/s; and (g,h) for U = 18.8m/s.*

above $U = 15.9$m/s, the signs of chaotic oscillations are clearly seen: the phase-plane is no longer defined by a single loop, and a dominant frequency is absent, as seen in Fig. 20(e) and (f). Therefore, the AR = 4 foil periodic regime ranges from 9.0 to 15.9m/s, which is a wide range of flow speeds, and it is promising for energy harvesting.
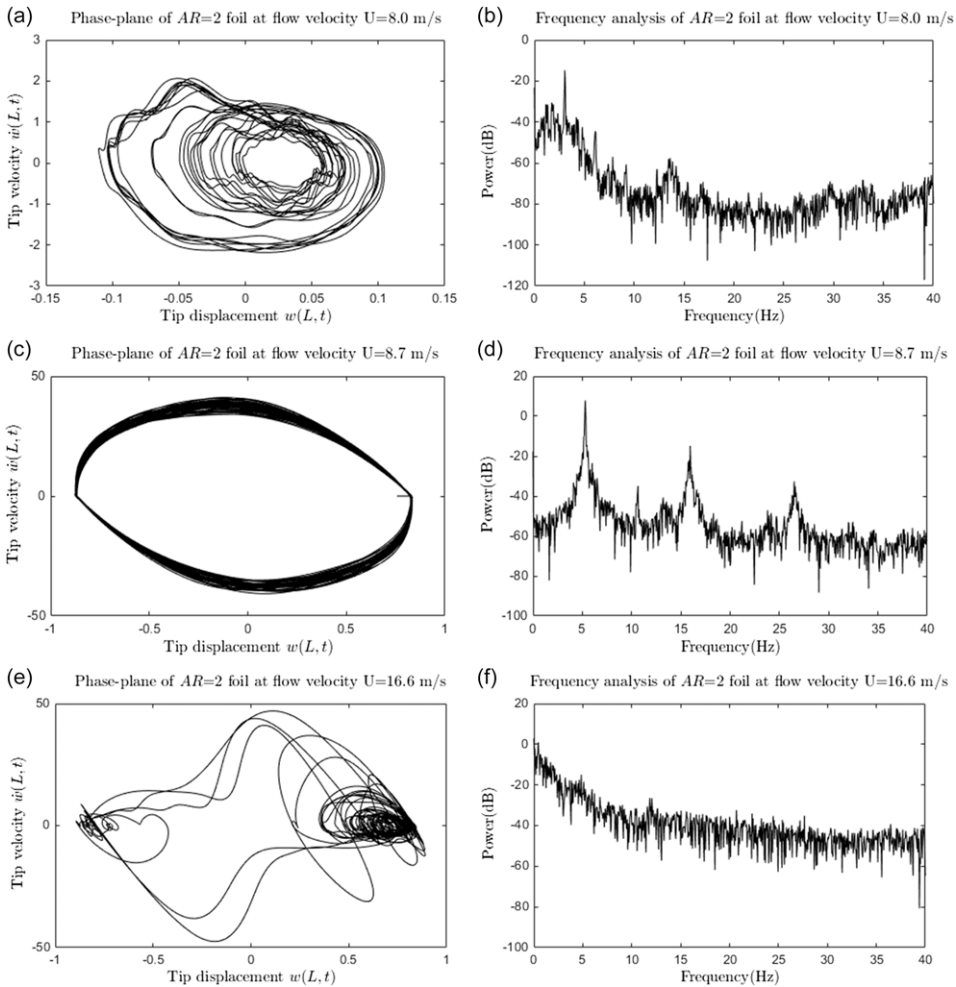
Figure 18. *(a,b) Phase-plane and frequency of $AR=2$ foil for $U=8.0 m/s$; (c,d) for $U=8.7 m/s$; and (e,f) for $U=16.6 m/s$.*

4.5 Dynamic regimes of the $0.5 \leq AR \leq 4$ inverted foils

The bifurcations of Poincaré maps allow the six regimes identified previously to be observed in a single graph for each foil size [37]. Figure 21 shows the six possible regimes encountered by the $AR=0.50$ foil as a function of the flow speed. The large-amplitude regime is wide before the foil's surface fully deflects.

The bifurcation diagram for the $AR=0.75$ foil, shown in Fig. 22, presents well-defined regimes, with a fully deflected foil after a flow value of 18m/s.

For the two foils with $AR=0.5$ and $AR=0.75$, the small-amplitude regime was around $\approx$10.0 m/s, but for $AR=1$, the foil passes suddenly from a straight position to full-amplitude oscillations. (This figure is not shown for brevity.)

The regimes for $AR=2$, $AR=3$ and $AR=4$ foils are presented in the bifurcations shown in Figs. 23, 24 and 25, respectively. We can observe that, with increasing AR, the critical wind speed at which the large amplitude regime initiates, is diminished. The critical flow speed for foils with AR>1 is smaller than $\sim$8m/s, which is significantly different from that for $AR=0.5$ and $AR=0.75$ (that is larger than 10m/s). Another interesting feature observed is that for the foils with $AR=0.5$ and 0.75

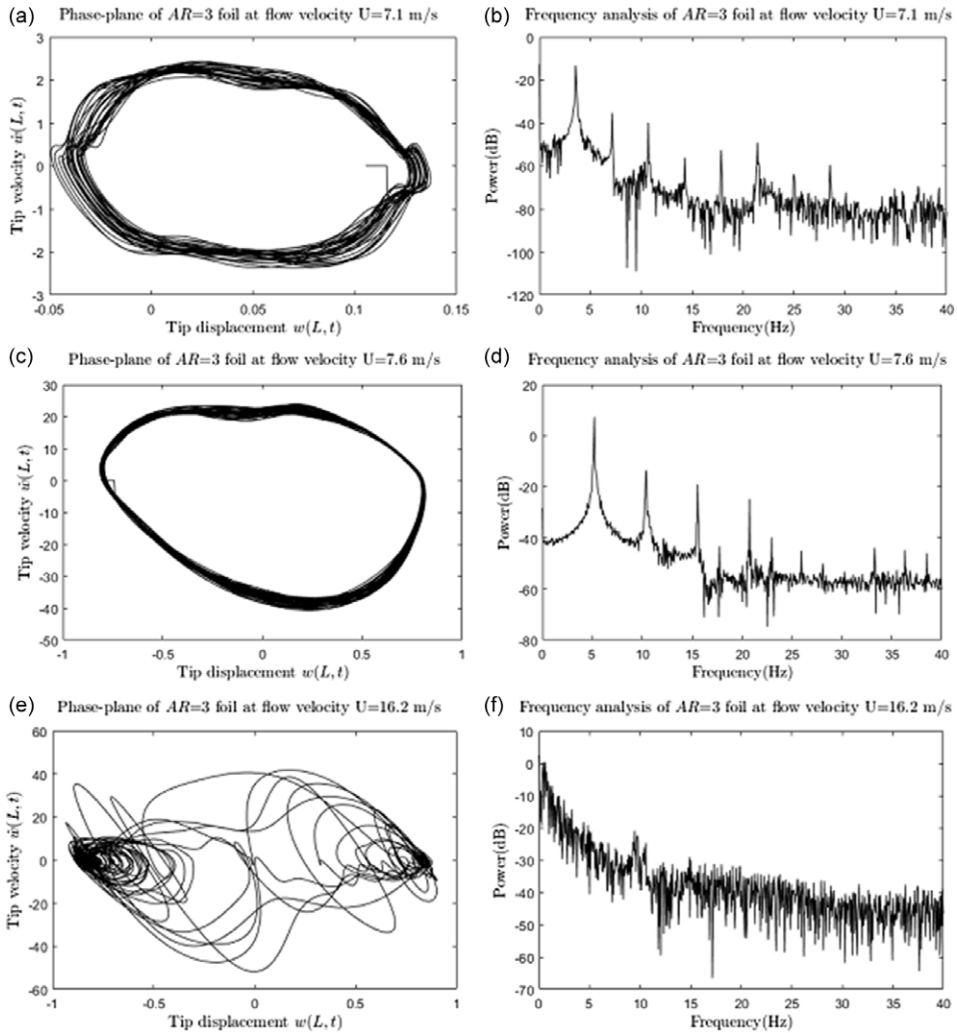**Figure 19.** *(a,b) Phase-plane and frequency of AR = 3 foil for U = 7.1m/s; (c,d) for U = 7.6m/s; and (e,f) for U = 16.2m/s.*

the chaotic regime lasts longer. Thus, for larger foils (AR > 1), the foil transitions fairly quickly from a large-amplitude regime to a fully deflected regime.

4.6. Forces and moments for 0.5 ≤ AR ≤ 4 inverted foils

The aerodynamic scale designed for the experiments enabled us to measure the forces and moments of six polycarbonate foils with aspect ratios in the range $0.50 \leq AR \leq 4$ and with a mass ratio $\mu = 0.15$.

The foil with aspect ratio $AR = 0.5$ can produce forces up to 8 Newtons during the large-amplitude regime in the flow regime $Re = 1.1 \times 10^5$.

The force and moment measurements for the transition between the straight regime and the large-amplitude regime can be observed in Figs. 26, 27, 28 and 29. For the $AR = 0.75$ foil, the force produced was much higher, as it increased to $Fx = 35N$ and $Fy = 38.5N$ in the large-amplitude regime
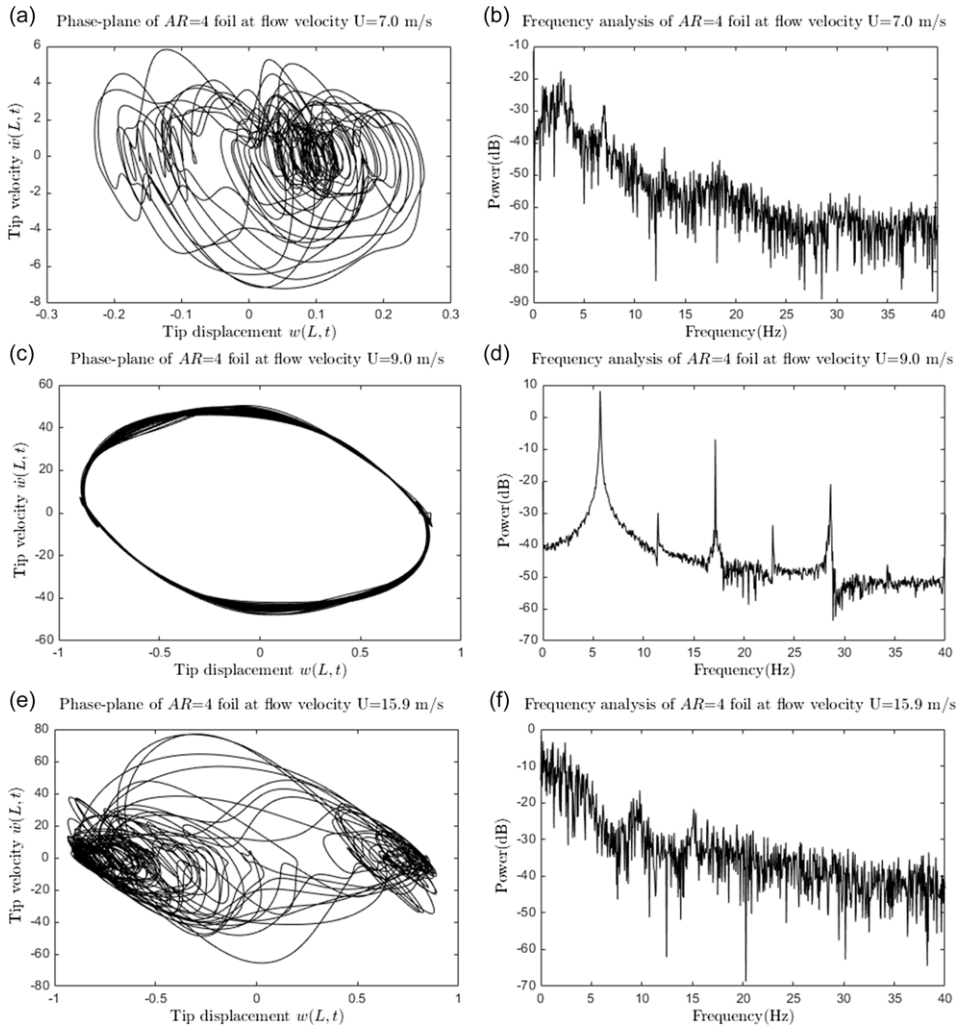
Figure 20. *(a,b) Phase-plane and frequency of AR=4 foil for U=7.0m/s; (c,d) for U=9.0m/s; and (e,f) for U=15.9m/s.*

range. Figure 26 shows how the forces and moments increase fairly quickly as soon as the foil starts flapping.

For a foil with an AR of 1, the forces Fx and Fy produced are close to 60N for the whole large-amplitude regime, and seem to be synchronised. The forces and moments develop gradually as the foil transitions from the stretched-straight regime to the large-amplitude regime.

The transition from the straight regime to the large-amplitude regime observed in Fig. 23 for an $AR=2$ foil can be also observed in the graph of forces Fx and Fy shown in Fig. 27. For this foil, the forces and moments did not increase considerably, but remained very close to those of the $AR=1$ foil, 40N for Fx and 3.5Nm and 3.0Nm for the moments Mx and My, respectively. The force Fy for $AR=2$ foil was lower than that of the $AR=1$ foil.

The $AR=3$ foil developed the largest forces and moments among all six foils; as the foil reached the large-amplitude regime, the forces measured were $Fx \approx 125$N and $Fy \approx 65$N and the moments were $Mx \approx 9$Nm and $My \approx 8$Nm. This foil produced the largest forces during the large-amplitude regime, until

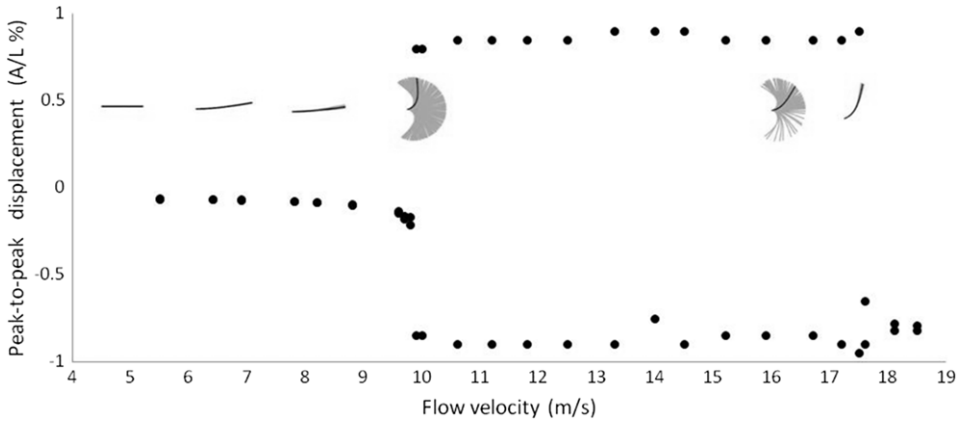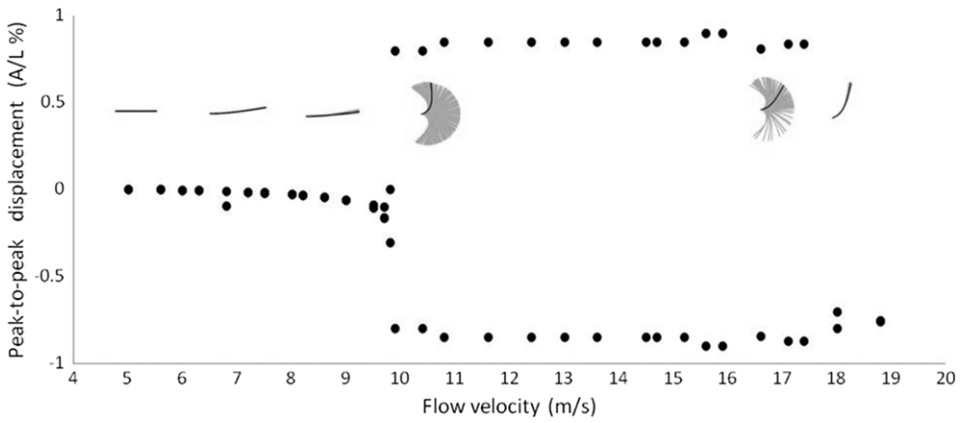**Figure 21.** *Bifurcations of Poincaré points for AR = 0.50 foil.*

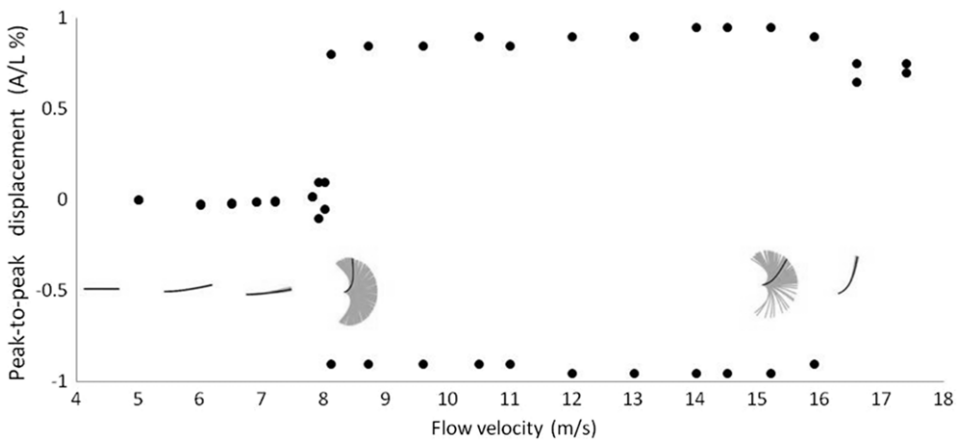**Figure 22.** *Bifurcation of Poincaré points for AR = 0.75 foil.*

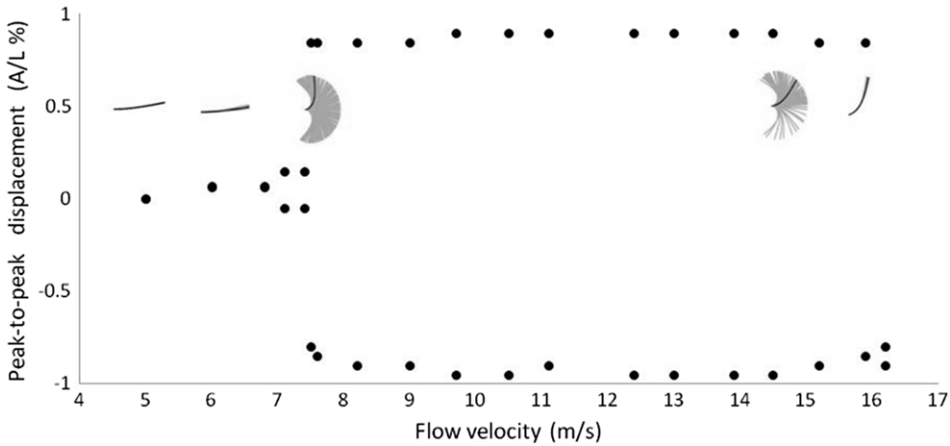**Figure 23.** *Bifurcation of Poincaré points for AR = 2 foil.*

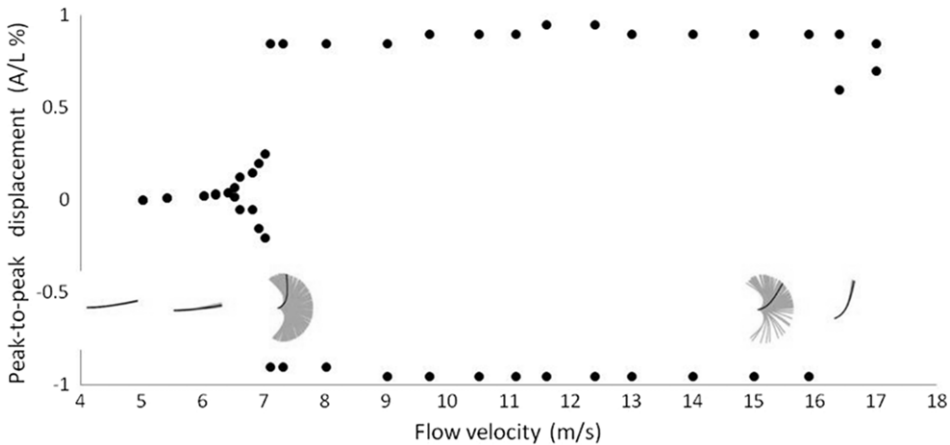**Figure 24.** *Bifurcation of Poincaré points for AR = 3 foil.*

Figure 25. *Bifurcation of Poincaré points for AR = 4 foil.*

it reached the fully deflected regime. Figure 28 shows the high forces produced by the oscillation of this flexible foil.

The last foil with AR = 4, exhibits smaller forces Fx and Fy and moments compared to the AR = 3 foil in the large-amplitude regime. Figure 29 shows that the AR = 4 foil does not produce constant forces. For the large-magnitude regimes of AR = 3 and AR = 4 foils, even if the foil deflection displays a full amplitude of $0.8L$, the maximum numerical values forces Fx produced by the AR = 4 foil are 56% less than the Fx forces produced by the smaller AR = 3 foil. (Calculation: Table 3: AR = 3 foil, $Fx = 125N$ and AR = 4 foil, $Fx = 70N$; *125N × 56% is equal to 70 N*. For the AR = 4 foil, Fx is 56% of Fx of the AR = 3 foil.)

4.7 Power and force generation

We examined the effects of Re and AR on the flapping regimes, and particularly on the Fx and Fy force generation, as these forces are very important to maximise energy harvesting. It was observed, when calculating the power output $\bar{P}$, that a large-amplitude regime, high oscillation frequency and a Strouhal number of 0.14 maximised the energy production of the foil.
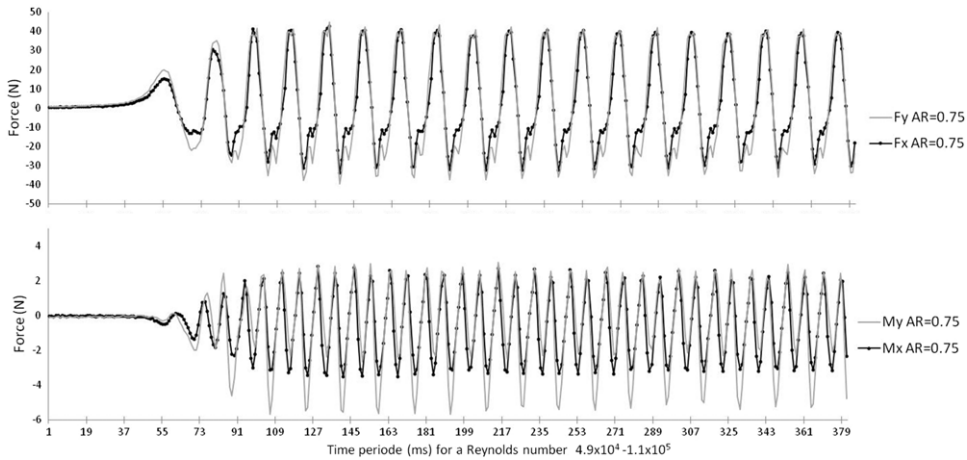
Figure 26. *Forces Fx and Fy and moments Mx and My for the AR = 0.75 foil for a Reynolds flow range* $4.9 \times 10^4 \leq Re \leq 1.1 \times 10^5$.
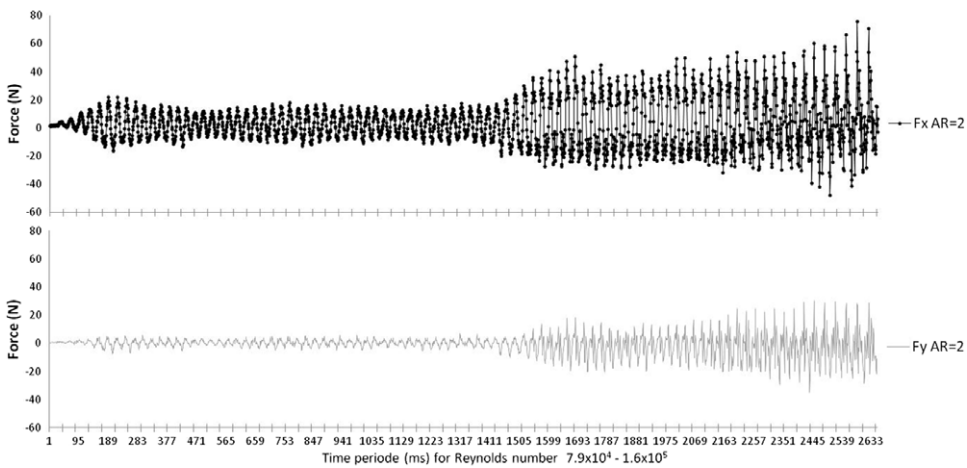

Figure 27. *Forces Fx and Fy for the AR = 2 foil for a Reynolds flow range* $7.9 \times 10^4 \leq Re \leq 1.6 \times 10^5$.

The work on harvested energy performed by Mitcheson [20] applied to inverted foils shows that the harvested power $\bar{P}$ is proportional to the amplitude times the cube of the frequency, as shown in Equation (1). The amplitude corresponds to the tip displacement of the foil, and the frequency of vibration of a blunt body is given by the Strouhal number. Thus, large amplitude with a high Strouhal number would increase the output power. The output power calculated for each foil is presented in Table 2.

The energy harvesting performance of six foils in the inverted foil configuration was analysed. The inverted foil with AR = 3 is best for maximising energy harvesting production, because: (i) the inverted foil configuration oscillates over a relatively large range of flow speeds, providing sustained power generation over a large wind speed range, as seen in Table 2; (ii) it can produce up to 1.06mW of output power, which is the second-highest amount of power generated by the six foils tested. The AR = 4 foil displays spanwise motion which can lead to a deterioration of the energy generation capability of the foil.

Table 3 shows the forces (*Fx*, *Fy*) and moments (*Mx*, *My*) generated by the six inverted-foils during the large-amplitude regime. Large-amplitude flapping with a constant frequency is the most effective
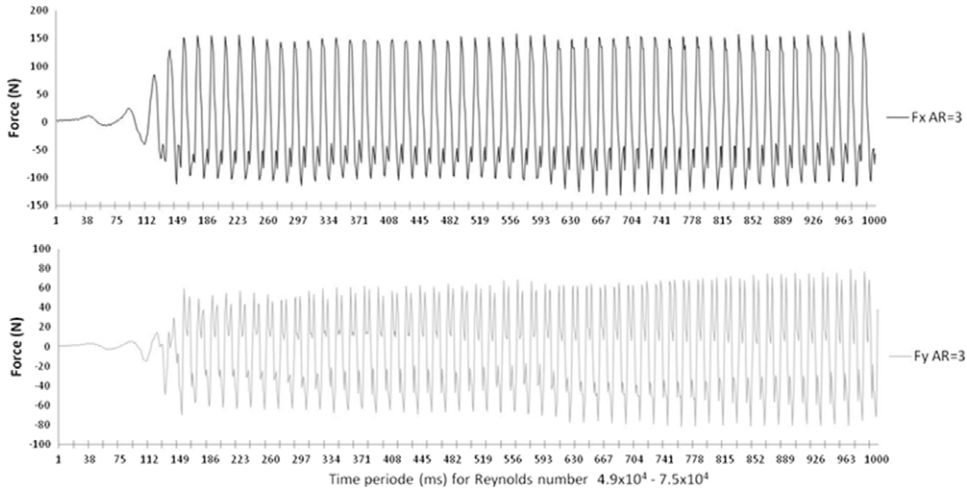
Figure 28. *Forces Fx and Fy for the AR = 3 foil for a Reynolds flow range* $4.9 \times 10^4 \leq Re \leq 7.5 \times 10^4$.
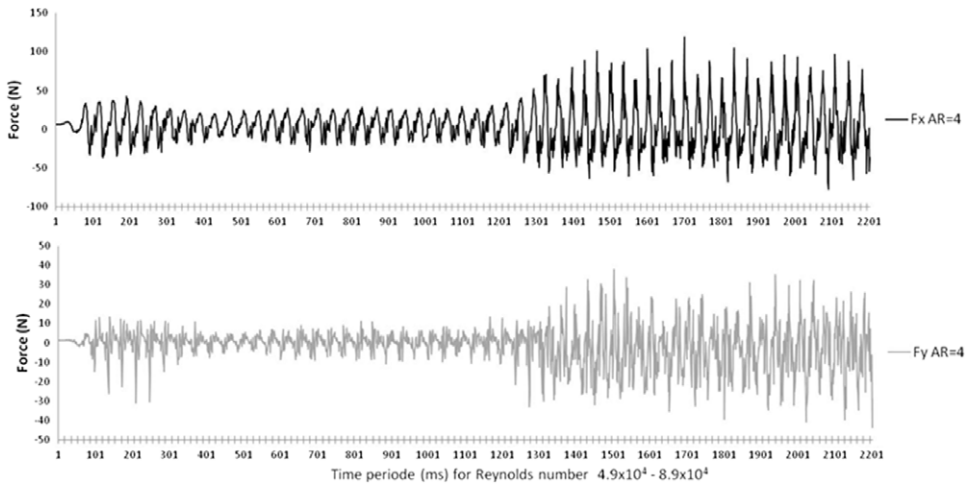

Figure 29. *Forces Fx and Fy for the AR = 4 foil for a Reynolds flow range* $4.9 \times 10^4 \leq Re \leq 8.9 \times 10^4$.

condition to produce large quantities of force from flexible foils in the inverted foil configuration. The AR = 3 foil is optimal for force and moment generation, as obtained experimentally and shown in Table 3.

The results discussed in this section show that the inverted-foil is capable of power generation over a wide range of flow regimes under realistic wind environments. The main characteristics of flapping of an inverted foil are: (i) the flapping regimes occur over a wide range of flow velocities, which makes them suitable for wind energy harvesting in realistic wind conditions with fluctuating flow speeds, as shown in Table 3; (ii) the peak-to-peak amplitude is large, leading to a high magnitude of stress on the surface of the foil, and therefore to a high output of energy production, as shown in Table 2.

It should be mentioned that using a foil configuration and a clamping mechanism different from the one presented in this study (Fig. 3), could affect greatly the foil's energy generation performance.

Table 2. *Power generation as function of inverted-foil aspect ratio*

Aspect Ratio	0.50	0.75	1	2	**3**	4
Output Power (mW)	0.494	0.299	0.650	0.956	**1.06**	1.07

Table 3. *Frequencies, forces Fx, Fy and moments Mx, My generation in terms of foil AR and fluid velocity during large-amplitude regime*

AR	*U*(m/s)	*f*(Hz)	*Fx*(N)	*Fy*(N)	*Mx*(Nm)	*My*(Nm)
0.5	10.0	5.3	4.5	6	0.25	0.4
0.75	11.6	5.2	35	38.5	0.25	0.4
1	9.1	4.85	60	60	3.0	7.0
2	8.78	5.3	40	25	3.5	3.0
3	**7.6**	**5.2**	**125**	**65**	**9.0**	**8.0**
4	9.0	5.7	70	22.5	4.0	5.0

5.0 Conclusion

In this article, we presented experimental results for flexible foils of different aspect ratio for the purpose of optimising energy harvesting. We presented the foils' experimental data in Poincaré bifurcation diagrams, in which the variation of the foil's displacement was shown as a function of increased flow speeds. In addition, the forces and moments at the foil's surface, the time-histories, probability density functions (PDF), phase-plane portraits and power spectral density (PSD) plots were presented for different Reynolds numbers to help understanding the foil's dynamics for energy harvesting purposes. This paper also investigated the evolution of the flapping instability as a function of some pertinent parameters, including flow speed, flapping frequency, Reynolds number, aspect ratio, bending rigidity and force production.

We investigated the energy harvesting capabilities of flexible foils in the inverted-foil configuration. More specifically, we focused on a wide range of foil sizes, $0.5 \leq AR \leq 4$, at high Reynolds number regimes of $10^4 \leq Re \leq 10^5$ in well-defined and controlled experimental tests. Through a series of wind tunnel tests, we studied the range of wind speed in which the flapping instability occurs. Additionally, we showed that the power generation capability of inverted foils increases with AR, and tends to converge to a certain value. Then, we identified the optimum AR foil for sufficient power generation with predominantly chordwise motion. Moreover, the present study allowed us to characterise the foil regimes, detect the critical flow speed to maximise energy harvesting performance, and measure, in real-time, the generated flapping forces and moments. The measurements suggest that foils with aspect ratio equal to 3, in the inverted-foil configuration, seem to be viable candidates for producing clean and renewable energy via small remote devices.

References

[1] Matlock, J., Warwick, S., Sharikov, P., Richards, J. and Suleman, A. Evaluation of energy efficient propulsion technologies for unmanned aerial vehicles, *Trans. Can. Soc. Mech.* 2019 Jun 4; **43**, (4), pp 481–489.

[2] Stockbridge, C. and CerutiMarzocca, A.P. Airship research and development in the areas of design, structures, dynamics and energy systems, *IJASS,* 2012, **13**, (2), pp 170–187.

[3] Afonso, F., Ferreira, A., Ribeiro, I., Lau, F. and Suleman, A. On the design of environmentally sustainable aircraft for urban air mobility, *Transp. Res. D Transp. Environ.* 2021 Feb 1, **91**, pp 102688.

[4] Alam, M.M., Chao, L.M., Rehman, S., Ji, C. and Wang, H. Energy harvesting from passive oscillation of inverted foil, *Phys. Fluids*, 2021 Jul 15, **33**, (7), p 075111.

[5] Allen, J. and Smits, A. Energy harvesting EEL, *J. Fluids Struct.*, 2001, **15**, pp 629–640.

[6] Dunnmon, J.A., Stanton, S.C., Mann, B.P. and Dowell, E.H. Power extraction from aeroelastic limit cycle oscillations, *J. Fluids Struct.*, 2011 Nov 1, **27**, (8), pp 1182–1198.

[7] Rostami, A.B. and Armandei, M. Renewable energy harvesting by vortex-induced motions: Review and benchmarking of technologies, *Renew. Sustain. Energy Rev.*, 2017 Apr 1, **70**, pp 193–214.

[8] Nabavi, S. and Zhang, L. Portable wind energy harvesters for low-power applications: A survey, *Sensors,* 2016 Jul, **16**, (7), p 1101.

[9] Machado, L., Matlock, J. and Suleman, A. Experimental evaluation of a hybrid electric propulsion system for small UAVs, *Aircr. Eng. Aerosp. Technol.,* 2019 Dec 2.

[10] Guo, C.Q. and Païdoussis, M.P. Stability of rectangular plates with free side-edges in two-dimensional inviscid channel flow, *J. Appl. Mech.*, 2000 Mar 1, **67**, (1), pp 171–176.

[11] Kim, D., Cossé, J., Huertas Cerdeira, C. and Gharib, M. Flapping dynamics of an inverted foil, *J. Fluid Mech.*, 2013, p 736.

[12] Sader, J.E., Huertas-Cerdeira, C. and Gharib, M. Stability of slender inverted flags and rods in uniform steady flow, *J. Fluid Mech.,* 2016, **809**, pp 873–894.

[13] Tavallaeinejad, M., Païdoussis, M., Salinas, M.F., Legrand, M., Kheiri, M. and Botez, R.M. Why inverted foils flap: An experimental study, In *Proceedings of 2nd International Symposium on Flutter and Its Application*. Paris, France 2020, May, pp 217–226.

[14] Tavallaeinejad, M., Païdoussis, M., Legrand, M. and Kheiri, M. Instability and the post-critical behaviour of two-dimensional inverted foils in axial flow, *J. Fluid Mech.,* 2020, **890**, p A14.

[15] Tavallaeinejad, M., Païdoussis, M., Flores Salinas, M., Legrand, M., Kheiri, M. and Botez, R. Flapping of heavy inverted foils: A fluid-elastic instability, *J. Fluid Mech.*, 2020, **904**, p R5.

[16] Yu, Y., Liu, Y. and Chen, Y. Vortex dynamics behind a self-oscillating inverted flag placed in a channel flow: Time-resolved particle image velocimetry measurements, *Phys. Fluids*, 2017 Dec 20, **29**, (12), p 125104.

[17] Zhao, W., Païdoussis, M.P., Tang, L., Liu, M. and Jiang, J. Theoretical and experimental investigations of the dynamics of cantilevered flexible plates subjected to axial flow, *J. Sound Vib.*, 2012, **331**, (3), pp 575–587.

[18] Chen, D., Gu, C., Zhang, R., Liu, J., Guo, D. and Marzocca, P. Vortex-induced vibrations of two degrees-of-freedom sprung cylinder with a rotational nonlinear energy sink: A numerical investigation. *J. Comput. Nonlinear Dyn.*, 2021 Jul 1, **16**, (7).

[19] Hu, G., Tang, L., Das, R. and Marzocca, P. A two-degree-of-freedom piezoelectric energy harvester with stoppers for achieving enhanced performance, *Int. J. Mech. Sci.*, 2018 Dec 1, **149**, pp 500–507.

[20] Mitcheson, P.D., Yeatman, E.M., Rao, G.K., Holmes, A.S. and Green, T.C. Energy harvesting from human and machine motion for wireless electronic devices, *Proc. IEEE*, Sep. 2008, **96**, (9), pp 1457–1486.

[21] Grigorie, L.T., Botez, R.M. and Popov, A.V. How the airfoil shape of a morphing wing is actuated and controlled in a smart way, *J. Aerosp Eng.*, 2015, **28**, p 04014043.

[22] Koreanschi, A., Sugar Gabor, O. and Botez, R.M. Drag optimization of a wing equipped with a morphing upper surface, *Aeronaut. J.*, 2016, **120**, pp 473–493.

[23] Tchatchueng Kammegne, M.J., Grigorie, L.T., Botez, R.M. and Koreanschi, A. Design and wind tunnel experimental validation of a controlled new rotary actuation system for a morphing wing application. *Proc. Inst. Mech. Eng. Part G. J. Aerosp. Eng.*, 2016, **230**, pp 132–145.

[24] Sugar Gabor, O., Koreanschi, A. and Botez, R.M. Optimization of an unmanned aerial system wing using a flexible skin morphing wing, *SAE International Journal of Aerospace*, 2013, **6**, 115–121.

[25] Botez, R.M. Morphing wing, UAV and aircraft multidisciplinary studies at the Laboratory of applied research in active controls, avionics and aeroservoelasticity LARCASE, *Aerospace Lab. ONERA*, 2018, **14**, (2), pp 1–14.

[26] Sugar Gabor, O., Koreanschi, A. and Botez, R.M. Analysis of UAS-S4 Éhecatl aerodynamic performance improvement using several configurations of a morphing wing technology, *Aeronaut. J.*, 2016, **120**, pp 1337–1364.

[27] Koreanschi, A., Sugar-Gabor, O., and Botez, R.M. Numerical and experimental validation of a morphed wing geometry using Price-Païdoussis wind tunnel testing. *Aeronaut. J.*, 2016, **120**, pp 757–795.

[28] Salinas, M.F., Botez, R.M. and Gauthier, G. New numerical and measurements flow analyses near radars, *J. Appl. Mech.*, 2021, **2**, pp 303–330.

[29] Mosbah, A.B., Salinas, M.F., Botez, R.M. and Dao, T.M. New methodology for wind tunnel calibration using neural networks-EGD approach, *SAE Int. J. Aerosp.*, 2013, **6**, (2), pp 761–766.

[30] Communier, D., Salinas, M.F., Carranza Moyao, O. and Botez, R.M. Aero-structural modeling of a wing using CATIA V5 and XFLR5 software and experimental validation using the Price-Païdoussis wing tunnel. In *AIAA Atmospheric Flight Mechanics Conference*, 2015, pp 2558.

[31] Barlow, J.B., Rae, W.H. and Pope, A. *Low-speed Wind Tunnel Testing*, 3rd ed. John Wiley and Sons, New York, USA, 1999.

[32] Technical information of the FLIR camera. Available online: https://www.flir.ca/products/grasshopper3-gige/ (accessed on Saturday, March 18, 2023).

[33] USB6210 Data Acquisition Card Module manual. Available online: https://www.ni.com/pdf/manuals/375194d.pdf (accessed on Monday, October 18, 2021).

[34] Poirel, D. and Mendes, F. Experimental small-amplitude self-sustained pitch–heave oscillations at transitional Reynolds numbers, *AIAA,* 2014 Aug, **52**, (8), pp 1581–1590.

[35] Poirel, D., Harris, Y. and Benaissa, A.M. Aeroelastic dynamics of a NACA 0012 airfoil in the transitional Reynolds number regime, *ASME PVP,* 2006 Jan 1, **47888**, pp 847–854.

[36] Tavallaeinejad, M., Salinas, M.F., Païdoussis, M.P., Legrand, M., Kheiri, M. and Botez, R.M. Dynamics of inverted foils: Experiments and comparison with theory, *J. Fluids Struct.*, 2021, **101**, p 103199.

[37] Poirel, D. and Price, S.J. Bifurcation characteristics of a two-dimensional structurally non-linear airfoil in turbulent flow, *Nonlinear Dyn.* 2007 Jun, **48**, (4), pp 423–435.